

DELFT UNIVERSITY OF TECHNOLOGY

FLOW MEASUREMENT TECHNIQUES

AE4180 2020/21

Laboratory Exercise Report

HWA & PIV

Submitted by:

Group 7

Aaron Sequeira (5258766)

Aniruddha Paranjape (5285143)

Jahnavi Raghavaraju (5312523)

Nikhil Joseph Jose (5321913)

Instructors:

Prof. A. Sciacchitano, Prof. F. Scarano

August 6, 2021



Contents

List of Figures	ii
List of Tables	ii
1 Introduction	1
2 Wind Tunnel Description and Experimental Apparatus	2
2.1 Wind Tunnel Description	2
2.2 Determination of Wind Tunnel Velocity	3
2.3 Experimental Apparatus	4
2.3.1 Model Specifications	4
2.3.2 Hot Wire Anemometry Instruments	4
2.3.3 Particle Image Velocimetry Instruments	4
3 Fundamentals	6
3.1 Hot Wire Anemometry	6
3.1.1 Working Principle	6
3.1.2 Simplified Static Analysis	7
3.2 Particle Image Velocimetry	8
4 Calibration and Setup	10
4.1 Hot Wire Anemometry	10
4.1.1 Hot Wire Anemometer Calibration	10
4.1.2 Overheat Ratio and Sampling Rate	11
4.2 Particle Image Velocimetry	12
4.2.1 Experimental Parameters	12
4.2.2 Redefined Parameters	15
5 Results	17
5.1 Hot Wire Anemometry	17
5.1.1 Mean Velocity and RMS Fluctuations	17
5.2 Particle Image Velocimetry	19
5.2.1 Results with Instructor Code	19
5.2.2 Results with Self-Made Code	27
6 Conclusion	30
6.1 Advantages of HWA and PIV	30
6.2 Disadvantages of HWA and PIV	31
6.3 Concluding Remarks on the Experiment	31

List of Figures

2.1	Experimental setup - W-Tunnel, High Speed Laboratory, TU Delft	2
2.2	Schematic of a Pitot-static probe	3
3.1	A basic HWA probe [4]	6
3.2	Experimental setup for PIV recording in a wind tunnel [1]	8
4.1	King's Law voltage-velocity curve fit.	10
4.2	A plot of the auto-correlation coefficient for various time lags.	12
5.1	Velocity profiles at $x = 1.2c$, obtained using hot-wire anemometry.	18
5.2	Instantaneous x -velocity contour computed at $\alpha = 0^\circ$	19
5.3	Statistical velocity contours computed at $\alpha = 0^\circ$	20
5.4	Instantaneous x -velocity contour computed at $\alpha = 5^\circ$	20
5.5	Statistical velocity contours computed at $\alpha = 5^\circ$	21
5.6	Instantaneous x -velocity contour computed at $\alpha = 15^\circ$, with $\Delta t = 100 \mu s$	22
5.7	Statistical velocity contours computed at $\alpha = 15^\circ$, with $\Delta t = 100 \mu s$	22
5.8	Statistical velocity contours computed at $\alpha = 15^\circ$, with $\Delta t = 6 \mu s$	23
5.9	Velocity profiles at $x = 1.2c$, obtained through both HWA and PIV.	24
5.10	Instantaneous x -velocity at $\alpha = 5^\circ$, for different interrogation window sizes.	25
5.11	Effect of the ensemble size on the velocity statistics.	26
5.12	Flowchart detailing the progression of the algorithm.	27
5.13	Instantaneous x -velocity contour computed at $\alpha = 15^\circ$, using a self-made PIV code.	28
5.14	Statistical velocity contours computed at $\alpha = 15^\circ$, using a self-made PIV code.	28
5.15	Velocity profiles at $x = 1.2c$, obtained using a self-made PIV code.	29

List of Tables

4.1	Maximum in-plane displacements based on interrogation window sizes	15
4.2	Maximum pulse separation based on interrogation window sizes at a freestream velocity of 10 m/s	15
4.3	Theoretical and Experimental Values of PIV Parameters	16

Chapter 1

Introduction

The laboratory exercise is an integral part of the course AE4180 Flow Measurement Techniques.

The experiment involves using velocimetry techniques for the investigation of the flow around a NACA 0012 airfoil at different angles of attack. The experiments are performed in the W-tunnel at the TU Delft High Speed Laboratory. The airfoil is installed in a closed test section built with transparent material for optical access. Two techniques will be used to study the flow around the airfoil, namely:

1. Hot Wire Anemometry (HWA)
2. Particle Image Velocimetry (PIV)

Fundamentally, a hot wire anemometer uses a fine wire that is electrically heated to above the ambient temperature. Air flowing past the wire cools it. Thus, a relationship can be obtained between the resistance of the wire and the speed of the air, since the resistance is dependant on the temperature. On the other hand, PIV is used to obtain instantaneous velocity measurements and other associated fluid properties. The fluid is seeded with tracer particles which are assumed to respect the flow conditions. The fluid, along with the particles, is illuminated so that particles are visible. The motion of the seeding particles is used to analyze the velocity field.

Due to COVID restrictions, the experiments were not performed by the group. Therefore, this report mainly focuses on analyzing and interpreting the results of the experimental data provided by the instructors. Chapter 2 describes the wind tunnel and the apparatus used to perform the experiment. Chapter 3 describes the principles behind HWA and PIV while Chapter 4 discusses specific calculations in the setup of both experiments, Chapter 5 delves into the results of the analysis, and a brief conclusion is presented in Chapter 6.

Chapter 2

Wind Tunnel Description and Experimental Apparatus

2.1 Wind Tunnel Description

The experiments are conducted in the W-tunnel at the High Speed Laboratory of the TU Delft. The W-tunnel is an open, low speed wind tunnel.

The inlet of the tunnel has the dimensions $2.0 \text{ m} \times 1.5 \text{ m} \times 2.0 \text{ m}$. Air is sucked into the inlet area by a fan that is driven by an electrical motor. For the PIV experiment, seeding particles are added to the flow in the inlet area to obtain a uniform particle distribution for accurate measurements. The air then passes through the diffuser which decelerates the flow. The nozzle exit has a cross-section area of $0.40 \text{ m} \times 0.40 \text{ m}$ [3].

From Laser Doppler Velocimetry data at 10.2 m/s , the RMS fluctuation in the axial direction was found to be less than 0.2% of the freestream velocity [3].

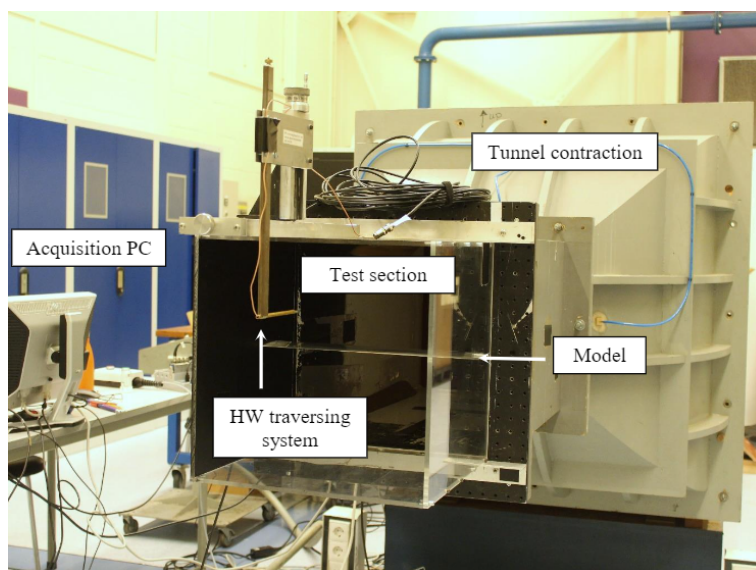


Figure 2.1: Experimental setup - W-Tunnel, High Speed Laboratory, TU Delft

2.2 Determination of Wind Tunnel Velocity

The velocity of the wind tunnel is quantified by means of a Pitot-static probe. The probe measures stagnation and static pressure of the flow. The velocity is then calculated using Bernoulli's principle, which states that an increase in fluid velocity occurs simultaneously with a decrease in pressure and vice versa. This can be written as:

$$P_o = P_s + P_d = P_s + \frac{1}{2}\rho U_\infty^2 \quad (2.1)$$

$$\Rightarrow U_\infty = \sqrt{\frac{2(P_o - P_s)}{\rho}} \quad (2.2)$$

where

P_o , P_s , P_d are the stagnation, static and dynamic pressures respectively

U_∞ is the free stream velocity

It is valid to assume that Bernoulli's principle can be applied here because the flow velocity of the wind tunnel is low enough to assume a steady, incompressible flow.

Figure 2.2 shows the schematic of a Pitot-static probe.

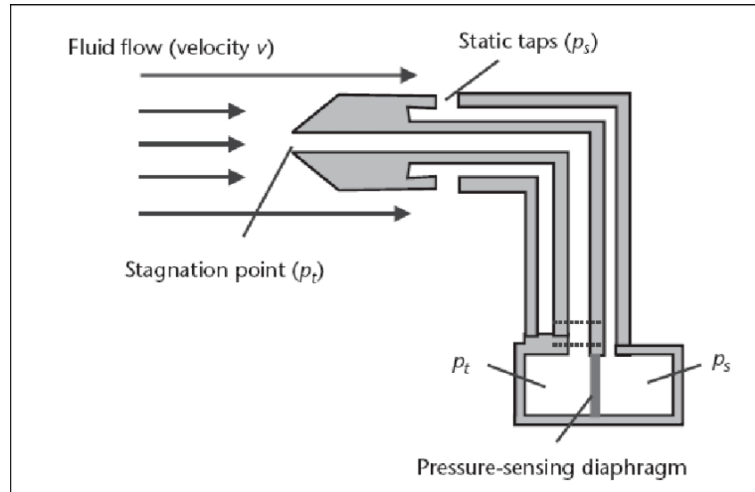


Figure 2.2: Schematic of a Pitot-static probe

The probe has two openings, one facing the flow and the other perpendicular to the flow direction. The first is used to measure the stagnation pressure (because the fluid reaches zero velocity at the head of the probe), and the latter is used to measure the static pressure. The pressure differential required to determine the flow velocity is measured using pressure transducers.

2.3 Experimental Apparatus

This section briefly looks at the apparatus used while performing both the experiments.

2.3.1 Model Specifications

The NACA number of the airfoil used is NACA 0012. This is a symmetric airfoil with a chord length of 10 cm. The model spans the width of the wind tunnel test section, i.e 40 cm. The airfoil is constructed out of plexiglas. The possible angles of attack are in the range of $\pm 30^\circ$, with the model being rotated about its quarter chord position.

2.3.2 Hot Wire Anemometry Instruments

Probe

The hot-wire probe is constructed out of an electrically conducting material. The wire is directly welded to the prongs and acts as the sensor. This sensor is introduced into the flow.

Constant Temperature Anemometer Bridge

The constant temperature anemometer bridge is a Wheatstone bridge consisting of four electrical resistances, of which one is the sensor mentioned above. The bridge works on its balancing principle. When the flow impinges on the sensor, the temperature of the probe changes, creating an imbalance in the bridge which is corrected by an amplifier. The resulting output voltage is used to indicate the flow velocity. The bridge is also used to set the correct overheat ratio.

Data Acquisition System

The raw voltage is acquired using a computer which stores the digital version of analog readings.

2.3.3 Particle Image Velocimetry Instruments

Seeding Generator

The seeding generator produces uniformly distributed fog containing water-glycol particles. This is produced by a machine after a brief heating period. The droplets are roughly $1\text{ }\mu\text{m}$ in diameter.

Laser

To illuminate the flow, a laser is used as the light source. The system used is a double pulsed Neodymium-doped Yttrium Aluminum Garnet (Nd: YAG) laser. Safety measures while handling the laser must be adhered to as it can damage the skin and eyes. The pulse energy is controlled by a computer, which can also trigger the camera through a Programmable Time Unit (PTU).

Camera

The PIV images are recorded with a Charged-Coupled Device (CCD) camera. The CCD has a resolution of 1628×1236 pixels with a pixel pitch of $4.40 \mu\text{m}$. The camera is controlled by the software that also controls the laser system.

PIV Software

For image acquisition and analysis, a computer software is used. This software has the following functions [3]:

1. Illumination and acquisition control (laser and camera settings)
2. Image analysis
3. Data post processing
4. Data display and output

Chapter 3

Fundamentals

3.1 Hot Wire Anemometry

In this section, we look at the fundamentals of Hot Wire Anemometry and its working.

Thermal anemometry is a method to measure fluid velocities by sensing the changes in heat transfer from a small, electrically heated sensor exposed to the fluid motion. The most common thermal anemometer is the hot-wire anemometer (HWA). A typical hot wire diameter is about $5\text{ }\mu\text{m}$ thick and 1 mm long.

3.1.1 Working Principle

The hot wire or the probe is made out of an electrically conducting metal/material. When an electrical current flows through it, it is heated due to resistance. This is the Joule effect, wherein electrical energy is converted into thermal energy through resistive losses in the material. In equilibrium, heat production is balanced by the heat lost to the flow (convective heat transfer). If the flow velocity changes, the amount of heat transfer changes and the wire temperature will change to eventually reach a new equilibrium.

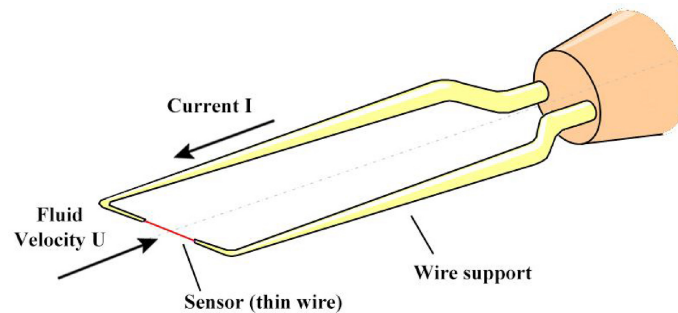


Figure 3.1: A basic HWA probe [4]

In this particular experiment, we use a constant temperature hot wire anemometer (CTA). In a CTA, a feedback controller will vary the current flowing in the wire such that the temperature of the wire remains constant. Thus, the fluid velocity can be determined from a relation between

the flow velocity and the the amount of current/voltage required to maintain the sensor at a constant temperature. This can be expressed as:

$$\frac{dE}{dt} = W - H \quad (3.1)$$

where

E is the thermal energy of the wire, given as $E = C_w T_S$

C_w is the heat capacity of the wire

W is the heat produced by the Joule effect mentioned above, given as $W = I^2 R_w$

H is the heat lost to the surroundings

Terms with the subscript 'S' relate to the properties of the surroundings while those with 'w' relate to those of the wire.

The heat lost to the surroundings is made up of three contributions:

$$H = Q_{\text{convection}} + Q_{\text{conduction}} + Q_{\text{radiation}} \quad (3.2)$$

3.1.2 Simplified Static Analysis

Under equilibrium conditions, heat storage in the wire is zero, as all the heat produced is lost to the flow in the form of conduction, convection and radiation, as per Equation 3.2. We make the following assumptions so that heat transfer due to conduction and radiation can be ignored:

- Negligible radiation losses
- Conduction between wire and support is minimal
- Uniform temperature distribution over the probe
- Velocity is impinged normally over the wire, which is of uniform composition
- Fluid temperature and density are constant during the experiment

Thus, we can say that:

$$\begin{aligned} W &= H = Q_{\text{convection}} \\ \implies I^2 R_w &= hA(T_w - T_f) \end{aligned} \quad (3.3)$$

We can introduce the Nusselt number, which is the ratio of the convective heat to the conductive transfer.

$$\text{Nu} = \frac{hd}{k_f} \implies I^2 R_w = \frac{\text{Nu } k_f}{d} A(T_w - T_f) \quad (3.4)$$

For forced convection:

$$\text{Nu} = A_1 + B_1 \text{Re}^n = A_2 + B_2 U^n \quad (3.5)$$

Where A_1, A_2, B_1 and B_2 are constants, U is the flow velocity and Re is the Reynolds number. n is the power that the velocity is raised to and depends on the system properties. These are determined by the calibration procedure. Thus, the heat balance equation is:

$$I^2 R_w = E^2 = [A_3 + B_3 U^n] A(T_w - T_f) \quad (3.6)$$

For constant T_w and T_f we can write the above equation as:

$$E^2 = A + BU^n \quad (\text{King's Law}) \quad (3.7)$$

We use the above principles and assumptions to process the data and compute the results of the experiment with Hot Wire Anemometry [2].

3.2 Particle Image Velocimetry

In this section, we look at the fundamentals of Particle Image Velocimetry and its working.

The principle of PIV is based on the measurement of the displacement of small tracer particles that are carried by the flow in a given time interval. The tracer particles must be sufficiently small to accurately trace the fluid path and not alter the properties of the flow instead. The tracer particles are illuminated within a thin light sheet generated from a pulsed laser, and the scattered light is then captured by cameras that are placed perpendicular to the measurement plane.

By analyzing the images taken by the camera, it is possible to determine the components of the flow velocity within the field defined by the light sheet. PIV is a non-intrusive measurement method, which contributes in making one of the most preferred methods to measure the flow velocity. However, it requires optical access to light up the particles and for the camera to take pictures. Additionally, accurate measurements require a high density of tracer particles and their homogeneous distribution within the observed flow region. The recorded images are typically analyzed by a computer software.

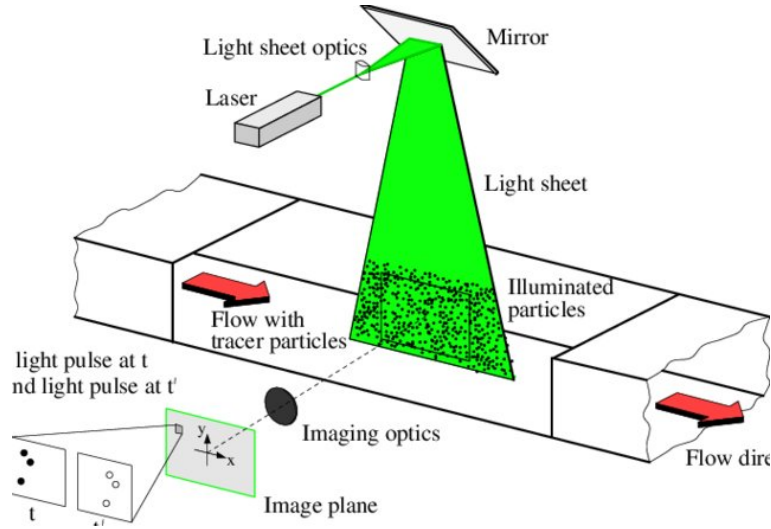


Figure 3.2: Experimental setup for PIV recording in a wind tunnel [1]

The analysis of the images is a cross-correlation analysis of the particle-image patterns in small sub-domains (interrogation windows) between the first and second image frame. The particle-image pattern displacement divided by the image magnification and the time delay between the laser light pulses yields the local fluid velocity. This process is then repeated for the entire domain, which gives us the instantaneous velocity in a planar cross-section of the observed flow.

The cross-correlation value of the interrogation windows indicates the degree of matching of the intensity distributions of the two windows. The position of the correlation peak indicates the average particle image displacement. The cross-correlation function is given as [2]:

$$\phi(m, n) = \frac{\sum_{i=1}^I \sum_{j=1}^J I(i, j) \cdot I'(i + m, j + n)}{\sqrt{\sum_{i=1}^I \sum_{j=1}^J I^2(i, j) \cdot I'^2(i, j)}} \quad (3.8)$$

In order to obtain the displacement vector, information is extracted from the interrogation windows. The two interrogation windows contain particle images which move from left to right in the time separation (Δt). The cross-correlation function ($\phi(x, y)$) exhibits a high peak, showing us the displacement made by the particles. Additional peaks may be present, which can be attributed to noise and correlation of non-paired particles.

Once the displacement vector is known, the velocity V , with components u along the freestream flow and v normal to the freestream flow, can be calculated as:

$$u = \frac{\Delta x \cdot \text{pxs}}{M \cdot \Delta t} \quad (3.9)$$

$$v = \frac{\Delta y \cdot \text{pxs}}{M \cdot \Delta t} \quad (3.10)$$

$$V = \sqrt{u^2 + v^2} \quad (3.11)$$

where

Δx is the displacement along the freestream flow

Δy is the displacement normal to the freestream flow

pxs is the pixel size of the camera being used

M is the magnification factor

Δt is the time interval between subsequent images

Chapter 4

Calibration and Setup

4.1 Hot Wire Anemometry

4.1.1 Hot Wire Anemometer Calibration

Figure 4.1 shows the calibration curve of the HWA. Since the probe is a constant temperature anemometer, the curve correctly follows the calibration trend of the CTA. This means that the voltage increases non-linearly as the velocity increases. This is because the faster moving flow takes away more heat from the wire by convection, meaning that more voltage (and current) is required to maintain the wire at its constant temperature.

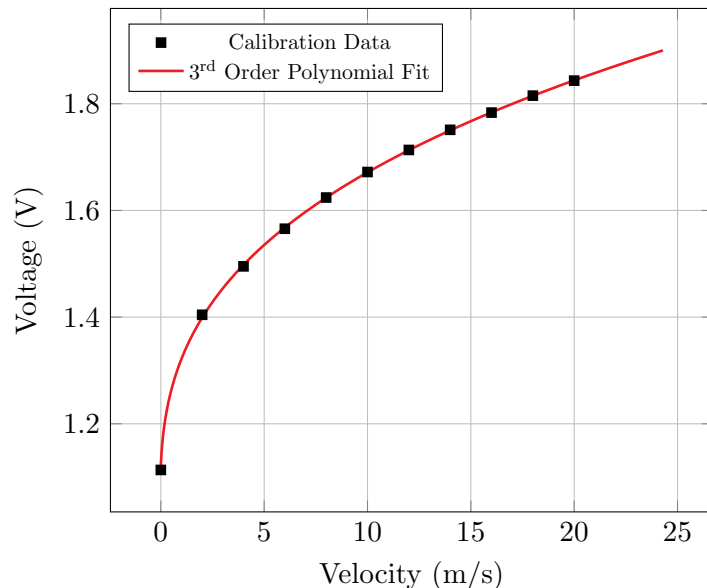


Figure 4.1: King's Law voltage-velocity curve fit.

For the calibration of the probe, the wind tunnel is run at a known velocity. This is measured by a pitot probe. For the set velocity, the corresponding values of voltage are recorded. This gives the experimental data-set required for the calibration. Curve-fitting is then employed to find the polynomial that best fits the data-set. It must be noted that the velocities should lie

in the range of experimental interest and must have a minimum of 5 measurements in order to be able to determine the coefficients of the polynomial (King's Law).

The data-set for the calibration is provided by the course instructors. The remainder of the procedure is performed on MATLAB. The `polyfit()` function is used to find the non-linear polynomial. `polyfit(x,y,n)` returns the coefficients for a polynomial $p(x)$ of degree n that is a best fit for the data in y by least square regression. In this case, we get the voltages for the given data-set of velocity. This is represented mathematically as:

$$U = C_0 + C_1.E + C_2.E^2 + C_3.E^3 + C_4.E^4 \quad (4.1)$$

From the definition of King's Law, we expect the velocity-voltage relation to be a 4th order non-linear relation. However, while calibrating, a 3rd order polynomial was found to have a better fit to the given calibration data.

4.1.2 Overheat Ratio and Sampling Rate

Overheat Ratio

Overheat ratio is the measure of the static response of the system. The resistance of the heated wire is proportional to the temperature difference between the heated wire and the wire at ambient conditions. This is quantified by the following expression:

$$R_h = R_a[1 + \alpha_0(T_h - T_a)] \quad (4.2)$$

where

R_h and T_h are the resistance and the temperature of the probe when heated

R_a and T_a are the resistance and the temperature of the probe at ambient conditions

α_0 is the temperature coefficient of resistance

This gives us the ability to model the response of the resistance of the wire in a manner that produces a clear and distinct voltage. This concept is used to set a parameter called the *overheat ratio*, which is mathematically written as:

$$\text{Overheat Ratio: } a = \frac{R_h - R_a}{R_a} = \alpha_0(T_h - T_a) \quad (4.3)$$

Simply put, the higher the value of the overheat ratio, the more sensitive the wire/probe will be. Thus, it is crucial that the correct overheat ratio is chosen during the experiment so that the velocity variations are correctly captured and the probe is not burnt out in doing so. For the current experiment, the overheat ratio was selected to be 0.5 [3].

Sampling Rate

The measurement frequency of the experiment must be set correctly so as to ensure a proper convergence of the velocity statistics. On one hand, sampling at too high a frequency can yield

unconverged statistics, while on the other hand, sampling at too low a frequency causes an increase in measurement time. To correctly identify the sampling frequency, we must identify the sampling frequency corresponding to a low autocorrelation coefficient.

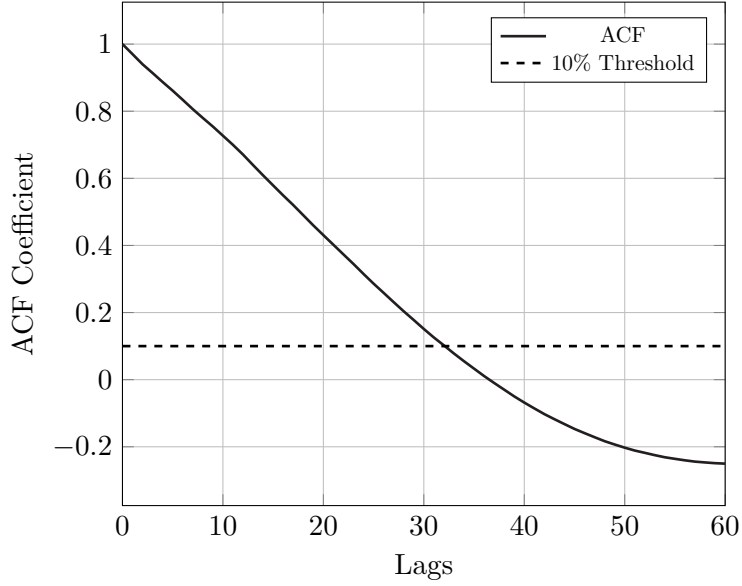


Figure 4.2: A plot of the auto-correlation coefficient for various time lags.

To collect the correlation data, the velocity of the wind tunnel is set to 10 m/s and the measurement is acquired for 10 seconds at 10 kHz. This data is then opened on MATLAB and processed using the `autocorr()` function. Auto-correlation is the correlation of a signal with a delayed copy of itself as a function of delay. The `autocorr()` function returns sample auto-correlated coefficient (`acf`) and the lag (`lags`). From this, a graph can be plotted between the returned values of the function against the lag. From the graph, we can determine the integral time scale for which the auto-correlation coefficient drops sufficiently below 0.1. From Figure 4.2, the integral time scale was found to be:

$$T_1 = 33 \times 1 \times 10^{-4} = 3.3 \text{ ms} \quad (4.4)$$

From this, the optimum sampling frequency can be calculated as:

$$f_{\text{opt}} = \frac{1}{2 \times 33 \times 1 \times 10^{-4}} = 151.5152 \text{ Hz} \quad (4.5)$$

4.2 Particle Image Velocimetry

4.2.1 Experimental Parameters

Field of View

The Field of View is the size of the region in the flow where it is being studied. In this case, we are required to capture 1.5 times the chord length of the airfoil. Given that the chord length

of the airfoil (c) is 10 cm, the Field of View is:

$$FOV = 1.5 \times c = 1.5 \times 0.1 = 0.15 \text{ m} \quad (4.6)$$

Magnification Factor

The Magnification Factor is the ratio of the image distance (d_i) to the object distance (d_o), expressed as:

$$M = \frac{d_i}{d_o} \quad (4.7)$$

It can also be expressed as the ratio between the size of the image captured by the sensor and the size of the object. In this case, the size of the object is given by the FOV while that of the image is given by the product of the pixel size and the number of pixels along the direction of the required FOV . Thus, we have:

$$M = \frac{\text{pixel size} \times \text{number of pixels}}{FOV} = \frac{4.4 \times 10^{-6} \times 1628}{0.15} = 0.04775 \quad (4.8)$$

Image and Object Distance

To determine the placement of the sensor and the lens with respect to the object, we calculate the image distance and object distance. This is given by the thin lens equation, written as:

$$\frac{1}{f} = \frac{1}{d_i} + \frac{1}{d_o} \quad (4.9)$$

The lens used for this activity has a focal length of 35 mm. Substituting the value of d_i from Equation 4.7 ($d_i = M \cdot d_o$) in Equation 4.9, we get:

$$\frac{1}{f} = \frac{1}{M \cdot d_o} + \frac{1}{d_o} = \frac{1}{d_o} \left(\frac{1}{M} + 1 \right) \quad (4.10)$$

Solving for d_o ,

$$d_o = f \left(\frac{1}{M} + 1 \right) = 35 \times \left(\frac{1}{0.04775} + 1 \right) = 767.98 \text{ mm} \quad (4.11)$$

Hence,

$$d_i = M \cdot d_o = 0.04775 \times 767.98 = 36.67 \text{ mm} \quad (4.12)$$

f-stop

f-stop is the ratio of the focal length of the lens to its aperture, expressed as:

$$f_{\#} = \frac{f}{d} \quad (4.13)$$

For the particle images to be focused, the laser sheet thickness should be smaller than the focal depth of the system, which is given by:

$$\delta z = 4.88 \lambda f_{\#}^2 \left(\frac{M+1}{M} \right)^2 \quad (4.14)$$

With a laser sheet thickness of 2 mm, this means that:

$$f_{\#} > \sqrt{\frac{\delta z}{4.88\lambda \left(\frac{M+1}{M}\right)^2}} = \sqrt{\frac{2 \times 10^{-3}}{4.88 \times 532 \times 10^{-9} \times \left(\frac{0.04775+1}{0.04775}\right)^2}} \quad (4.15)$$

$$\implies f_{\#} > 1.26 \quad (4.16)$$

Another criteria to be kept in mind while calculating $f_{\#}$ is the particle image diameter (d_{τ}), expressed as:

$$d_{\tau} = \sqrt{(Md_p)^2 + (d_{\text{diff}})^2} \quad (4.17)$$

where

d_p is the size of the particles in the flow (1 μm)

d_{diff} is the particle image diameter due to diffraction effects and is related to $f_{\#}$ as:

$$d_{\text{diff}} = 2.44\lambda(1 + M)f_{\#} \quad (4.18)$$

If the pixel size is larger than one particle image, *peak locking* or *pixel locking* occurs, wherein the particle position cannot be determined with subpixel accuracy. In this case, the position of a particle and its measured displacement can only have integer values. To prevent this, the particle image size is set to be 2 to 3 times the pixel size.

Solving for d_{diff} ,

$$d_{\text{diff}} = \sqrt{(d_{\tau})^2 - (Md_p)^2} \quad (4.19)$$

$$\implies d_{\text{diff}} > \sqrt{(8.8)^2 - (0.04775 \times 1)^2} \approx 8.8 \mu\text{m} \quad (4.20)$$

$$\text{and } d_{\text{diff}} < \sqrt{(13.2)^2 - (0.04775 \times 1)^2} \approx 13.2 \mu\text{m} \quad (4.21)$$

Rearranging Equation 4.18 and solving for $f_{\#}$,

$$f_{\#} = \frac{d_{\text{diff}}}{2.44\lambda(1 + M)} \quad (4.22)$$

$$\implies f_{\#} > \frac{8.8 \times 10^{-6}}{2.44 \times 532 \times 10^{-9}(1 + 0.04775)} = 6.47 \quad (4.23)$$

$$\text{and } f_{\#} < \frac{13.2 \times 10^{-6}}{2.44 \times 532 \times 10^{-9}(1 + 0.04775)} = 9.71 \quad (4.24)$$

Thus, from Equations 4.16, 4.23 and 4.24, we determine that $f_{\#}$ must lie between 6.47 and 9.71. It is evident that particle image diameter dictates the value of $f_{\#}$ over the laser sheet thickness.

Light pulse separation

The optimal interval between exposures is chosen such that most of the particles are captured in the same window in both exposures. An effective method to achieve this is using the one-quarter rule, which says that the maximum in-plane displacement should be smaller than $1/4^{th}$ of the interrogation window size. This can be written as:

$$\Delta x \leq \frac{\text{pixel size} \times \text{interrogation window size in freestream direction}}{4} \quad (4.25)$$

Thus, for different window sizes, the maximum in-plane displacements are as follows:

Table 4.1: Maximum in-plane displacements based on interrogation window sizes

Interrogation window size	Δx (μm)
16×16	17.6
32×32	35.2
64×64	70.4

The pulse separation can be written in terms of the in-plane displacement as:

$$\Delta t = \frac{\Delta x}{MV} \quad (4.26)$$

Substituting the values of the maximum in-plane displacements from Table 4.1 into Equation 4.26, we obtain the maximum pulse separation as follows:

Table 4.2: Maximum pulse separation based on interrogation window sizes at a freestream velocity of 10 m/s

Interrogation window size	Δt (μs)
16×16	36.86
32×32	73.72
64×64	147.43

4.2.2 Redefined Parameters

Upon performing the calibration of the system in the wind tunnel and processing it using the provided MATLAB script, it was found that the magnification factor was actually 0.04348, which is lesser than the theoretically obtained magnification factor as per Equation 4.7. It was decided to compute the results based on this magnification factor because:

- The calibration was performed using millimetre paper with clearly defined spatial markings.
- Using the theoretically obtained value yielded results where the freestream velocity was notably lower than 10 m/s.

Although it appears that the airfoil section is longer than the defined chord length, this can be attributed to perspective. The section whose image is being taken is 20 cm ahead of the section that is being illuminated and where the particles are passing through. Hence, this is not a matter of concern.

Using the experimentally obtained magnification factor, the parameters defined above are recalculated and displayed in the following table:

Table 4.3: Theoretical and Experimental Values of PIV Parameters

Parameter	$M_{theoretical}$ (0.04775)	$M_{experimental}$ (0.04348)
d_o	767.98 mm	839.97 mm
d_i	36.67 mm	36.52 mm
$f_{\#min}$	6.47	6.50
$f_{\#max}$	9.71	9.75
16×16	36.86 μs	40.48 μs
Δt_{max} 32×32	73.72 μs	80.96 μs
64×64	147.43 μs	161.91 μs

Chapter 5

Results

In this chapter, we look at and analyze the results that are obtained from the Hot Wire Anemometry and Particle Image Velocimetry experiments. The chapter is divided into two sections in which we describe the results in more detail.

5.1 Hot Wire Anemometry

5.1.1 Mean Velocity and RMS Fluctuations

In this section, we look at the results of the measurement campaign, during which we set the probe at $x = 1.2c$. The probe measures the velocity profile of the test model at three different angles of attack, namely: $\alpha = 0^\circ, 5^\circ, 15^\circ$. The hot-wire probe is made to traverse a distance of ± 40 mm by using the traversing system of the anemometer.

Initially, the probe is set to $y = -40$ mm and the wind tunnel is switched on to run at 10 m/s using the software. The measurement is acquired at the determined sampling rate. This procedure of data acquisition is then repeated for the for the traversal domain (± 40 mm) in increments of 4 mm and for all the predetermined angles of attack.

Figure 5.1a describes the mean velocity profile of the test model. As expected, increasing the angle of attack reduces the velocity behind the airfoil. This can be attributed to the flow separation that occurs at high angles of attack when the flow can't keep up with the adverse pressure gradient. For an angle of attack $\alpha = 0^\circ$, we get an almost symmetrical profile. This is expected as the airfoil is the symmetrical NACA 0012 airfoil. The minor deviations can be attributed to the spatial resolution of ± 4 mm. Further away from the center of the trailing edge, the flow returns to the freestream velocity of 10 m/s.

When the angle of attack is $\alpha = 5^\circ$, there is a reduction in velocity behind the airfoil. However, the reduction is seen more on the lower surface of the airfoil. This makes sense as the the positive angle of attack causes a pressure difference on the upper side and lower side of the airfoil, increasing the velocity over the airfoil while decreasing the velocity below it. Far away from the center of the trailing edge, we can see the flow returning to the freestream velocity. However, on the upper surface of the airfoil, we see that the flow is slightly higher than 10

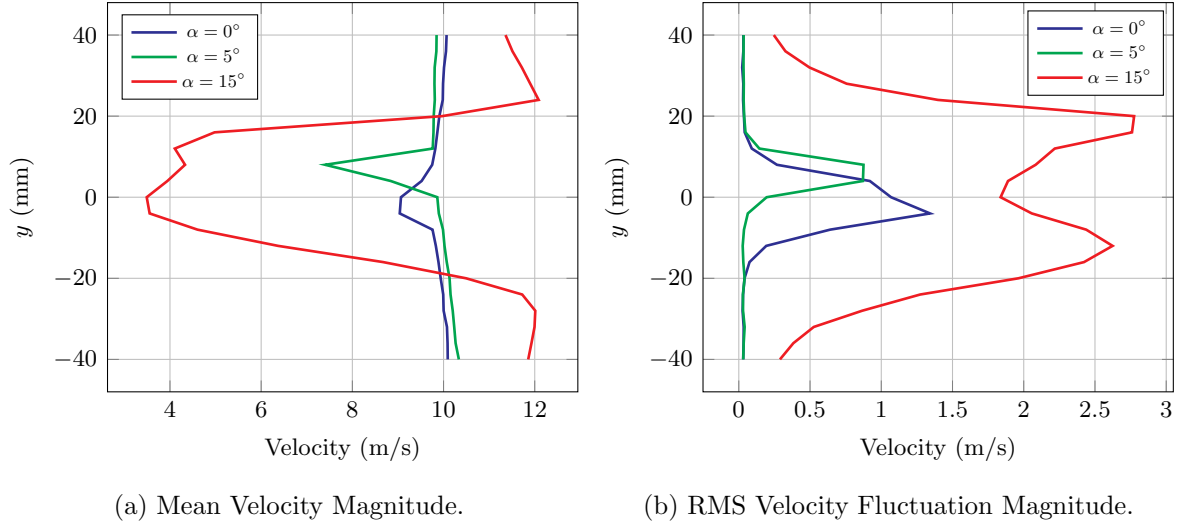


Figure 5.1: Velocity profiles at $x = 1.2c$, obtained using hot-wire anemometry.

m/s as a result of the acceleration over the upper surface. In the case of the angle of attack being $\alpha = 15^\circ$, we see that there is massive flow separation on the airfoil. This is also reflected in Figure 5.1a, in which the mean velocity of the flow is much much lower around the airfoil as compared to the $\alpha = 0^\circ, 5^\circ$ cases. The pressure difference is still not recovered away from the airfoil. These regions have a much higher velocity than the flow (10 m/s). This shows the extent of the adverse pressure gradient on the airfoil. Pressure recovery happens after ≈ 25 mm on either side of the airfoil.

The RMS velocity fluctuations can be explained in a similar fashion to the mean velocities. For the angles of attack $\alpha = 0^\circ, 5^\circ$ the RMS fluctuations quickly return to a negligible value. The RMS fluctuations are observed in a transverse region of ± 15 mm. This can be attributed to the boundary layer effects of the test model. For the case of the angle of attack being $\alpha = 15^\circ$, we see that the RMS fluctuations are much higher than the other cases. This can be attributed to the flow separation at high angles of attack and the ensuing turbulent flow in the wake of the airfoil.

5.2 Particle Image Velocimetry

5.2.1 Results with Instructor Code

In this section, we look at the data when it is processed by the code provided by the instructor. The results for this section are processed at angles of attack: $\alpha = 0^\circ, 5^\circ, 15^\circ$ with the results being categorized by the velocity contours at instantaneous x -velocities, mean velocities, and RMS velocities.

Angle of Attack = 0°

We first look at the case where the angle of attack is $\alpha = 0^\circ$. The images reflect the physics of the flow past a symmetric airfoil. The velocity distributions are nearly identical over and under the airfoil, and hence there is no pressure difference created between the suction and pressure sides of the airfoil. This is why at 0° , a symmetrical airfoil does not generate any lift.

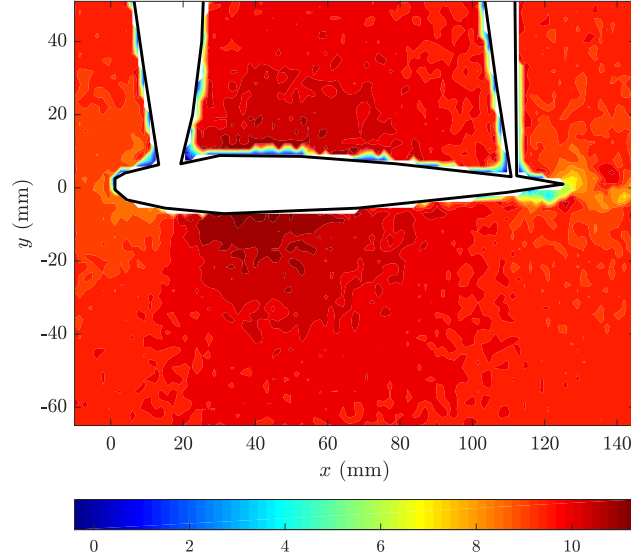


Figure 5.2: Instantaneous x -velocity contour computed at $\alpha = 0^\circ$.

In the above figure, we also notice some vortex formations at the trailing edge of the airfoil. This phenomenon can be attributed to Vortex Shedding. Vortex Shedding is an oscillating flow that takes place when a fluid flows around a body at certain velocities, depending on the size and shape of the body (Reynolds Number). In this regime, vortices are created at the back of the body and detach periodically from either side, forming a "Von Kármán vortex street". The flow past the body creates alternating low-pressure vortices. This could explain why the instantaneous velocity contour shows a small variation in the velocities close to the surface of the airfoil. This could also be attributed to the interference between the wind tunnel and the model. We do not add any type of corrections while processing the data.

Close to the airfoil, we see some velocity reduction, which can again be attributed to the presence of a boundary layer around the airfoil due to the flow.

The wake of the airfoil is better captured in the RMS fluctuations, which are of small velocity magnitudes, while the rest of the flow in the wind tunnel appears to be smooth with small residual turbulence.

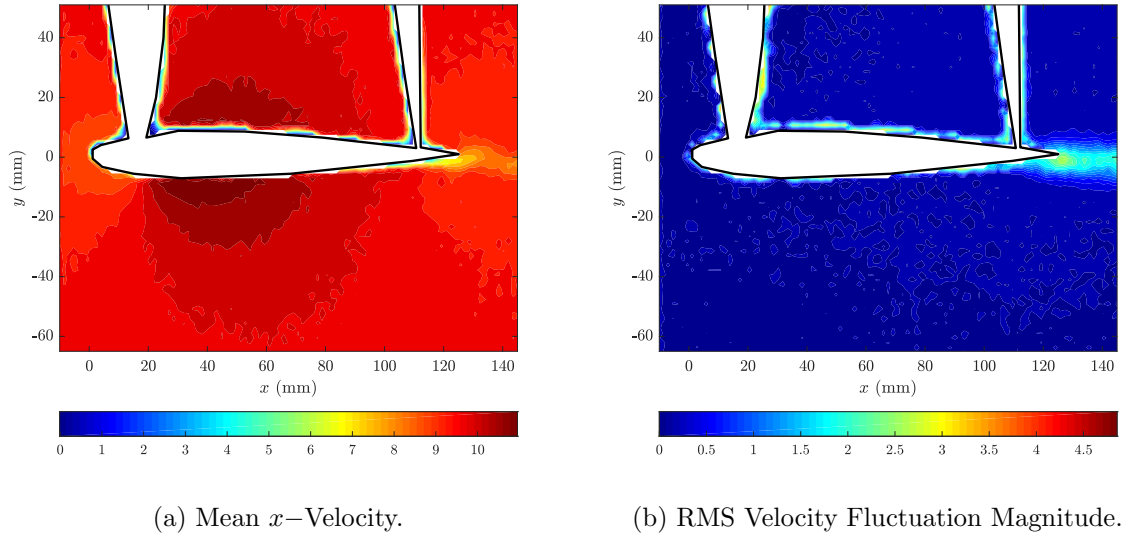


Figure 5.3: Statistical velocity contours computed at $\alpha = 0^\circ$.

Angle of Attack = 5°

In this section, we look at the case where the angle of attack is $\alpha = 5^\circ$. The images reflect the physics of the flow past a symmetric airfoil at a low to medium angle of attack. The velocity distributions is unequal over and under the airfoil, and hence there is a positive pressure gradient created between the suction and pressured side of the airfoil. This is why at 5° , a symmetrical airfoil generates lift.

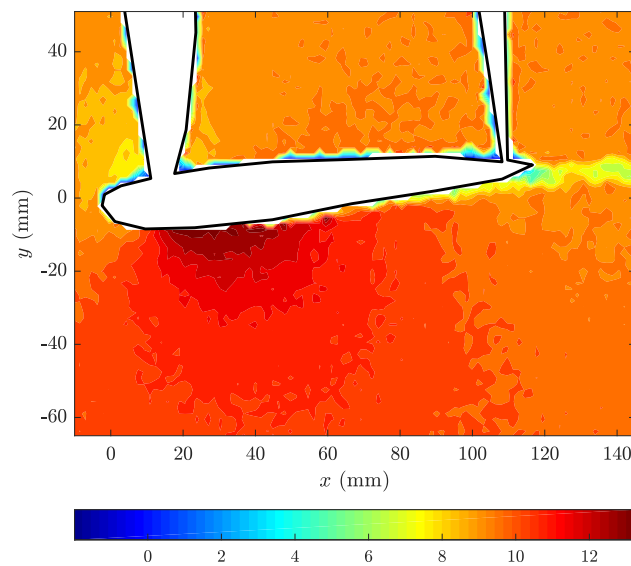


Figure 5.4: Instantaneous x -velocity contour computed at $\alpha = 5^\circ$.

Contrary to the previous case, the small angle of attack causes the velocity on the suction side of the airfoil to increase. On the other hand, the velocity on the pressure side of the airfoil falls a little. This velocity difference is observed through out the domain of the image. Another observable effect is the replacement of the oscillating wake with a much more straight wake with larger thickness.

Close to the airfoil, we see some velocity reduction, which can again be attributed to the presence of a boundary layer around the airfoil due to the flow.

The wake of the airfoil is better captured in the RMS fluctuations, which are of very small velocity magnitudes, while the rest of the flow in the wind tunnel appears to be smooth with small residual turbulence. This wake has a more laminar characteristic, in the sense that the RMS fluctuations in the wake are observably small and uniformly distributed throughout the width. This can be attributed to the small angle of attack it is fixed in. Since the angle of attack is small, the flow is able to overcome the adverse pressure gradient with relative ease and minimal flow separation.

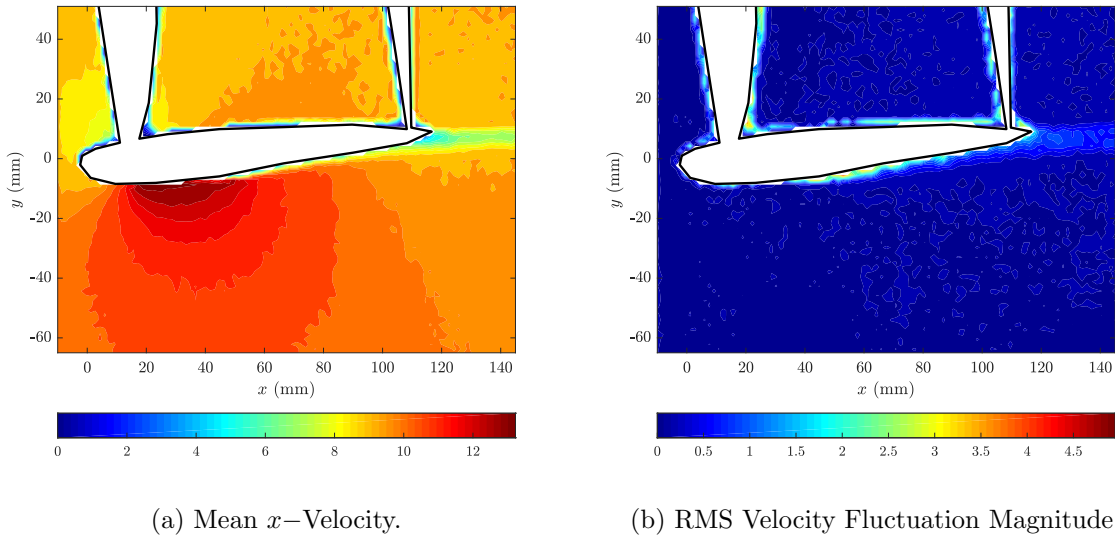


Figure 5.5: Statistical velocity contours computed at $\alpha = 5^\circ$.

Angle of Attack = 15°

In this section we look at the case where the angle of attack is $\alpha = 15^\circ$. The images reflect the physics of the flow past a symmetric airfoil at a very high angle of attack. The velocity distributions are unequal over and under the airfoil coupled with large flow separation on the suction side of the airfoil. This flow separation is detrimental to the ability of the airfoil to produce lift.

In the instantaneous velocity contour, we see a noticeable difference in the flow field in the airfoil's suction and pressure sides. However, on the suction side, we see massive flow separation. This is characterized by very low velocities and negative velocities in some cases. The negative

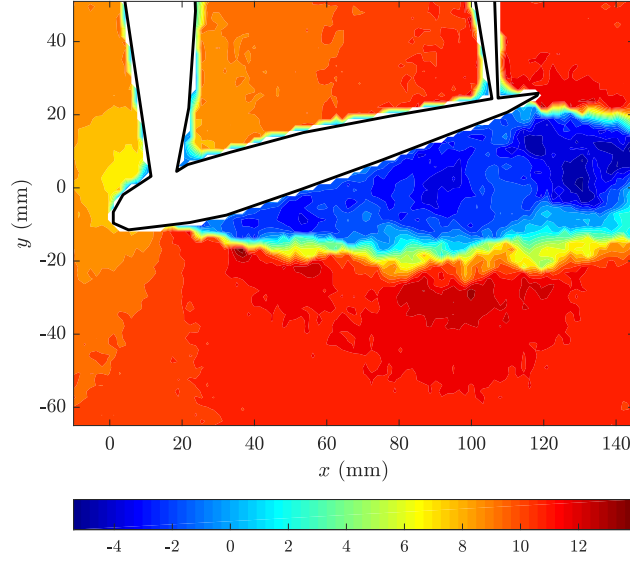


Figure 5.6: Instantaneous x -velocity contour computed at $\alpha = 15^\circ$, with $\Delta t = 100 \mu s$.

velocity simply indicates the existence of flow reversal. At very high angles of attack, the flow around the airfoil is subject to a very high adverse pressure gradient. Subjecting the flow to such adverse pressure gradients is akin to increasing the flow potential energy by reducing the flow kinetic energy (deceleration). The boundary layer around the airfoil is most affected by this phenomenon as it is already slower due to viscous effects close to the airfoil. Thus, for a high enough adverse pressure gradient, the local flow does not have enough kinetic energy to overcome it, and the flow can either come to rest, reverse or separate. This phenomenon affects the lift and drag characteristics of the airfoil.

We now look at mean and RMS velocity contours of the airfoil at $\alpha = 15^\circ$ with two different pulse separations, namely: $\Delta t = 100 \mu s$ and $\Delta t = 6 \mu s$.

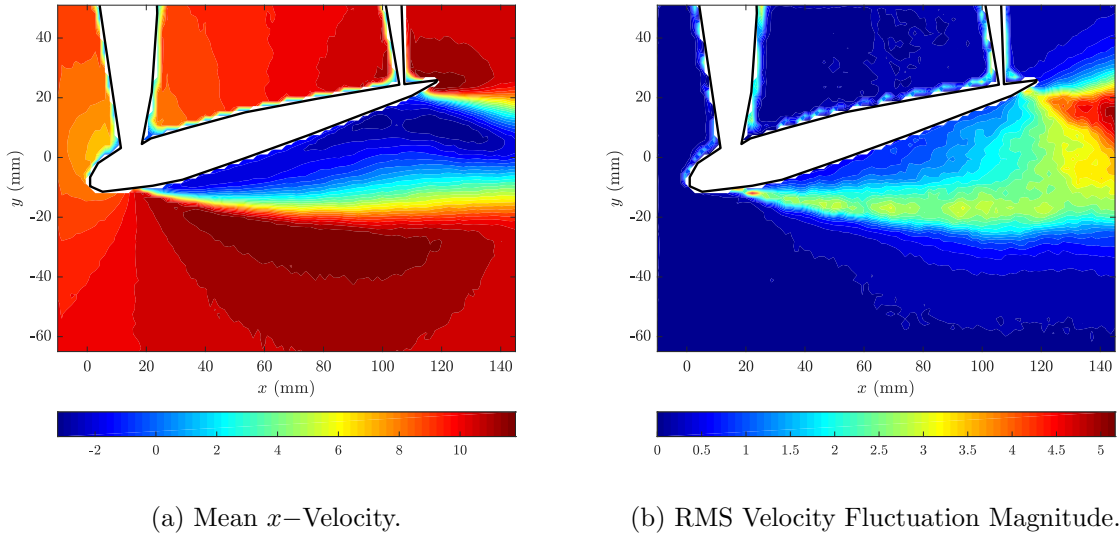


Figure 5.7: Statistical velocity contours computed at $\alpha = 15^\circ$, with $\Delta t = 100 \mu s$.

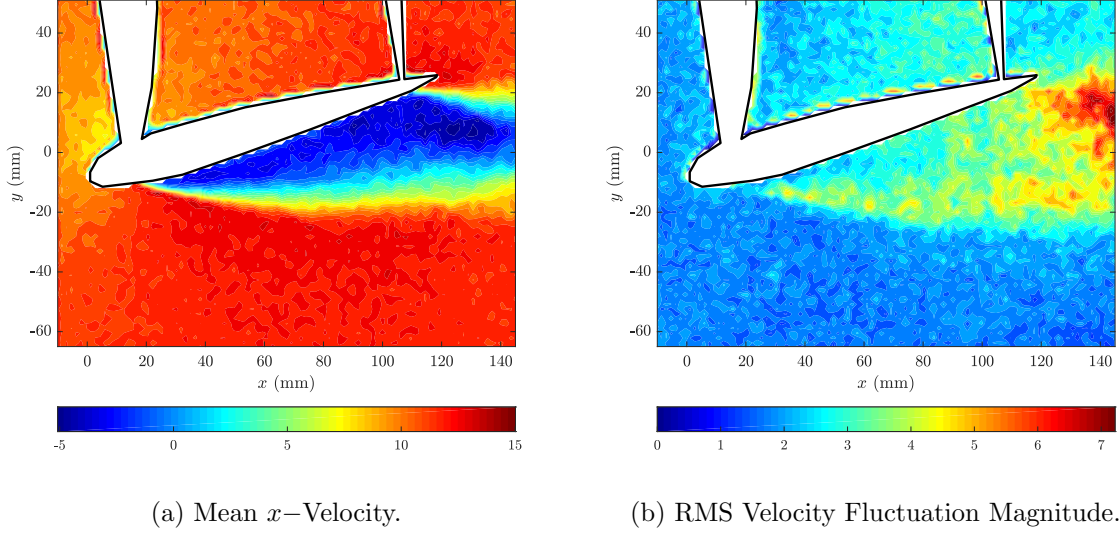


Figure 5.8: Statistical velocity contours computed at $\alpha = 15^\circ$, with $\Delta t = 6 \mu s$.

We see that in Figure 5.7, having a larger pulse separation results in the velocity contour being smoother as compared to Figure 5.8. The shorter pulse separation shows the micro variations in the velocity (this can also be said to be noise in the image) which are smoothed out by the longer pulse duration. It must be noted however, that having a pulse separation that is too long might result in the particles leaving the second image frame. If the pulse separation is too small, then there is uncertainty in the direction of the particles within the the flow. This makes it critical to choose an appropriate pulse separation, wherein the time is large enough to have certainty about the flow direction and small enough that most of the particles are retained between image frames. The trade-off must be made between spatial resolution and noise.

Velocity Profiles

In this section, we compare the results of hot wire anemometry and particle image velocimetry. The comparison is made at a position $x/c = 1.2$. The angles of attack being compared here are $\alpha = 0^\circ, 5^\circ, 15^\circ$.

We start this comparison at $\alpha = 0^\circ$. From the onset, we see that PIV predicts a higher reduction in velocity as compared to HWA. This can be attributed to PIV having higher spatial resolution as compared to HWA. This allows PIV to get a clearer picture of the wake. Another reason for the difference can be due to the earlier observed Von Kármán vortex street. The HWA probe being used can only measure the flow that is perpendicular to it and hence is limited in the ability to resolve flow structures such as the Von Kármán vortex street. The RMS values are closely matched between the two methods. However, PIV shows definitive peaks in the velocity profile. This can be attributed to the Von Kármán vortex street that is better captured by PIV.

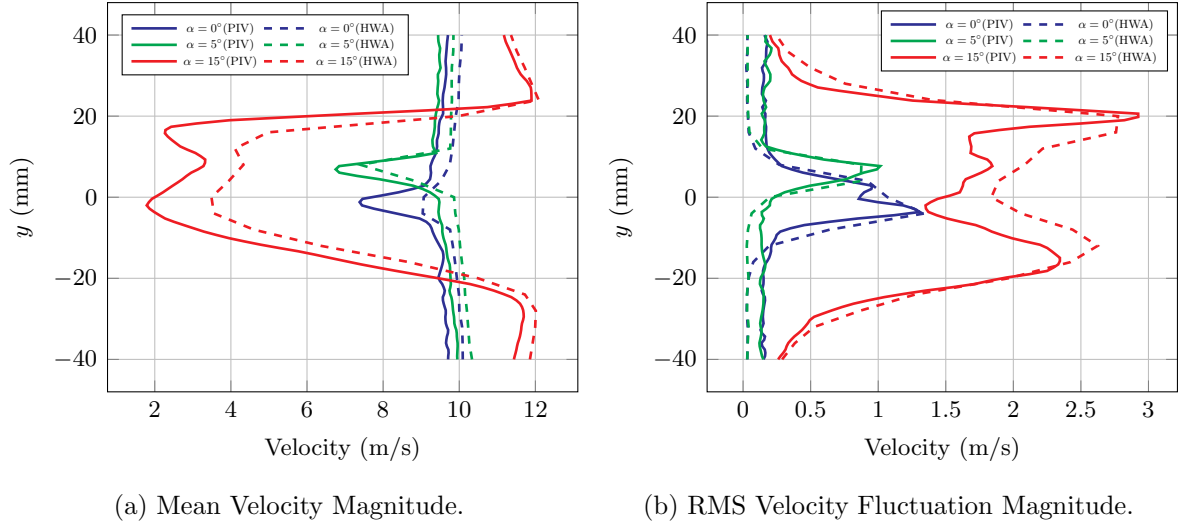


Figure 5.9: Velocity profiles at $x = 1.2c$, obtained through both HWA and PIV.

For the angle of attack of $\alpha = 5^\circ$, we see that the results of HWA and PIV are closely matched, although PIV does predict slightly higher values than HWA. This can again be attributed to lack of spatial resolution in HWA. However, the similarity of results can be attributed to the fact that the flow is generally smooth around the airfoil. The small angle of attack does not create a large adverse pressure gradient causing the flow to be smooth over the airfoil and the wake to have laminar characteristics with constant width. Hence, even the RMS fluctuations are closely matched in trends and values.

Finally, at the angle of attack of $\alpha = 15^\circ$, we see that the results of HWA and PIV are again very different. We see that PIV again predicts higher values of velocity than HWA, but also provides better details of the mean and RMS fluctuations. As discussed before, this can be down to not only the spatial discretization differences between the two, but also to the fact that HWA cannot perceive the flow direction. Since the hot wire probe only measures the temperature changes (and consequently voltage and velocity) it cannot distinguish the direction of the flow past the probe. This means that the flow reversal that occurs in the separated wake of the airfoil at high angles of attack is poorly captured, if not captured at all. This is one of the strengths of PIV and is reflected more in the RMS velocity profile where the peaks are better defined than HWA.

Sensitivity Study

This section looks into the significance of interrogation window size and ensemble size on the results. The effect of light pulse separation has been discussed in Section 5.2.1 (sub-section *Angle of Attack = 15^\circ*).

A crucial step in accurate data analysis is the selection of interrogation window size. Too large a window size causes a drop in spatial resolution while a value that is too small leads to erroneous results. Figure 5.10 visualises the instantaneous velocity for various window sizes and proves this claim. From Figure 5.10a, it is seen that using a window size of 16×16 px

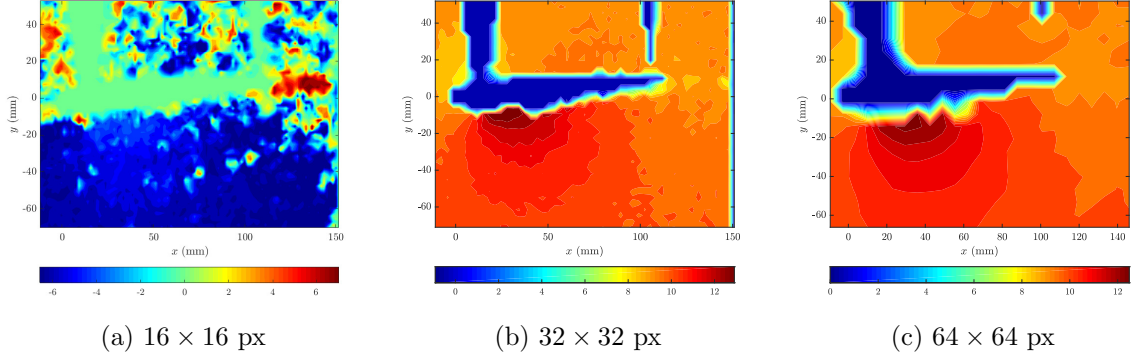
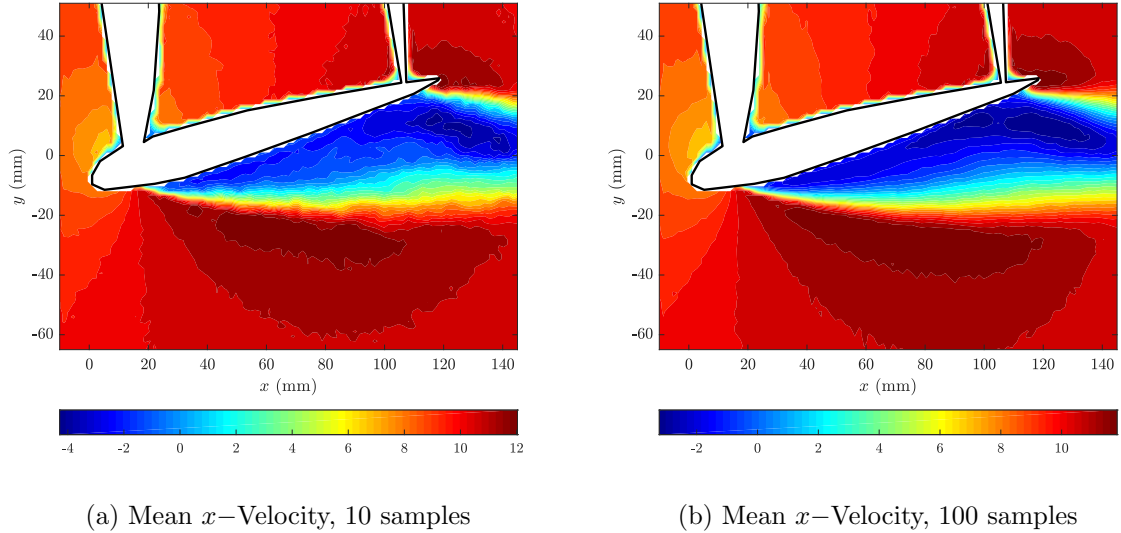


Figure 5.10: Instantaneous x -velocity at $\alpha = 5^\circ$, for different interrogation window sizes.

leads to a very noisy image with an unrealistic flow field. In fact, the velocity in most of the image appears to be negative, which is known to be false. This can be attributed to the fact that an insufficient number of particles are captured in a correlation window, meaning that the correlation function cannot track the displacement of these particles. Increasing the window size to 64×64 px yields much more realistic results in terms of the magnitudes of velocities observed in the flow. However, this comes at the cost of spatial resolution, seen in the form of highly jagged edges in Figure 5.10c. The ideal interrogation window size is found to be an intermediate value of 32×32 px. This offers a good trade-off between capturing an accurate flow field while maintaining satisfactory spatial resolution. As seen in Figure 5.10b, while there are a few rough edges with minor non-uniformities in the flow, the overall flow field is as expected with practical velocity magnitudes.



Another important parameter while analysing the captured images is the selection of the ensemble size, i.e. the number of image pairs from which velocity statistics are calculated. For this comparison, ensemble sizes of 10 and 100 samples are used. Comparing the mean x -velocities and the root-mean-squared velocity magnitude fluctuations for both ensemble sizes, it is apparent that the flow field in the laminar region looks similar in both cases. The difference lies in the turbulent wake region. The contours are seen to be smoother when the ensemble

size is larger, which is logical because the variations in the mean reduce when the sample size is larger.

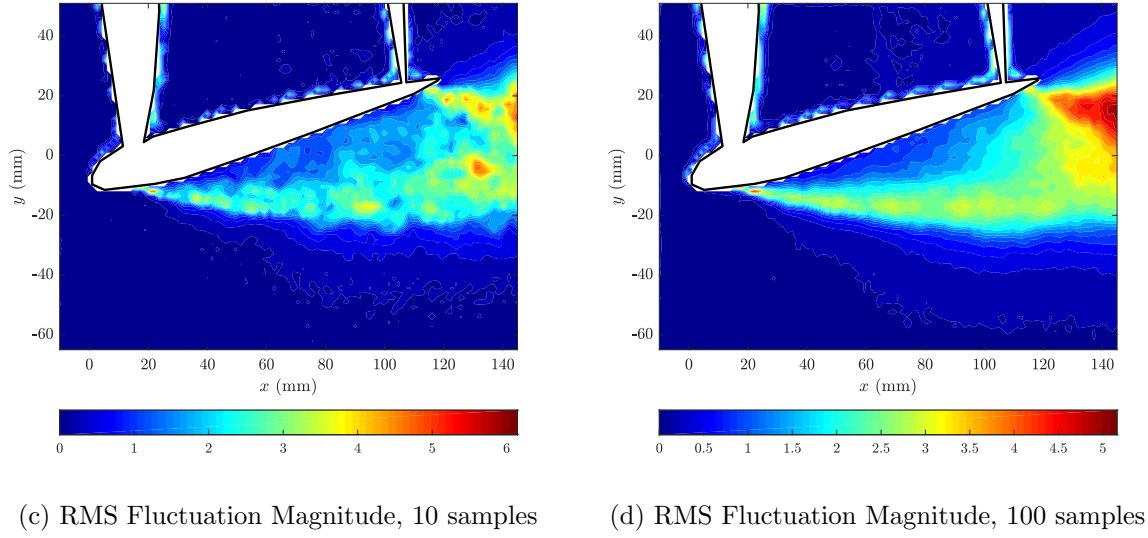


Figure 5.11: Effect of the ensemble size on the velocity statistics.

A similar pattern is seen when comparing the root-mean-squared velocity fluctuations. The velocity contours are smoother and more continuous when a larger ensemble size is chosen across the flow field. In the turbulent wake region, several pockets of high fluctuation are scattered when 10 samples are considered. When the ensemble size is increased to 100, this is seen as a more consistent high fluctuation zone, representing the shear layer between the outer laminar flow and the turbulent wake. This is likely due to a high degree of circulation and reversed flow, especially near the trailing edge, meaning that image pairs vary significantly from each other. Note that the peak fluctuation magnitude is higher when fewer samples are considered (the scales of the two figures are different).

Another point worth noting is that since only a few samples are considered, Figures 5.11a and 5.11c would look quite different if 10 other image pairs had been chosen.

5.2.2 Results with Self-Made Code

In addition to analysing the PIV image-pairs with code provided by the instructors, a self-made code was developed for the same. This section details the results of the PIV analyses carried out using the self-developed code.

Algorithm

The self-made code fundamentally makes use of cross-correlations to compute the velocity components within discrete interrogation windows, as with all PIV codes. This is done using MATLAB's `xcorr()` functionality. The image pairs are first masked to exclude the airfoil region from the computation process. They are then cropped and subdivided into interrogation windows of a selected size. The cross-correlation routine is then called whereby the program loops through all interrogation windows, correlating corresponding windows of the image pairs. The location of the cross-correlation peak is determined using a Gaussian peak-interpolation procedure. This location is then converted into velocity components using the prescribed magnification factor, pixel size and pulse-separation time. The flow of the self-made PIV code and its subroutines is highlighted in the following flow chart.

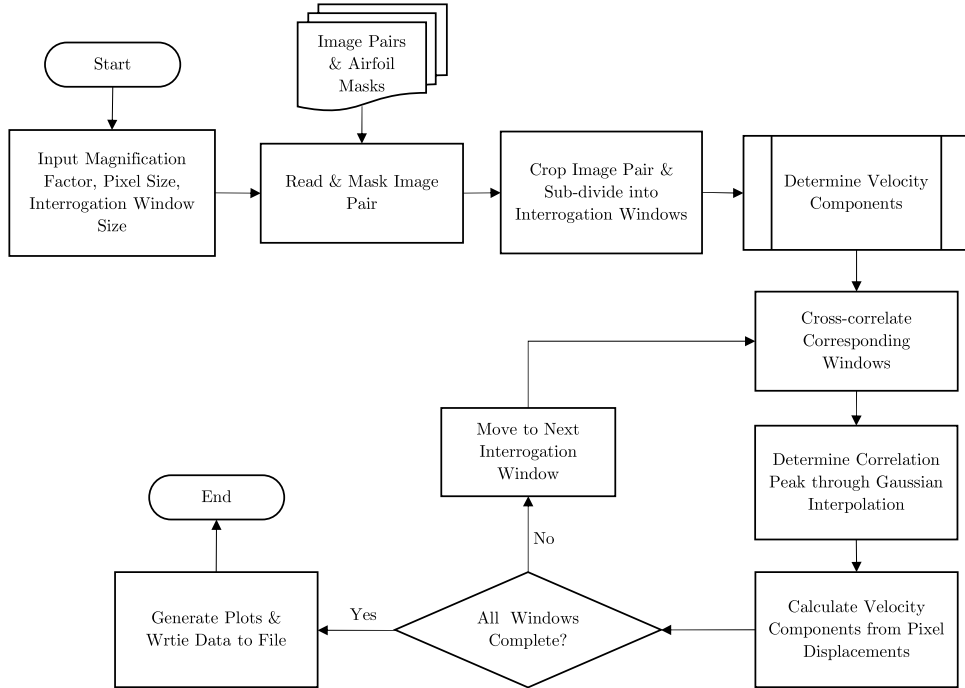


Figure 5.12: Flowchart detailing the progression of the algorithm.

Flow Contours

In this section, we look at the case where the angle of attack is $\alpha = 15^\circ$, obtained from the self-made PIV code. The pulse-separation time is $\Delta t = 100 \mu s$. The instantaneous velocity contour is shown in figure 5.13. The suction side shows massive flow separation, which is characterised by very low velocities and negative velocities as seen before. The negative velocities are indicative of flow reversal. However, when compared to the instructor code, the velocities predicted on the

suction side have a higher value. We can also observe slightly jagged edges which are a result of the algorithm ignoring cross-correlation peaks that lead to spurious velocity values.

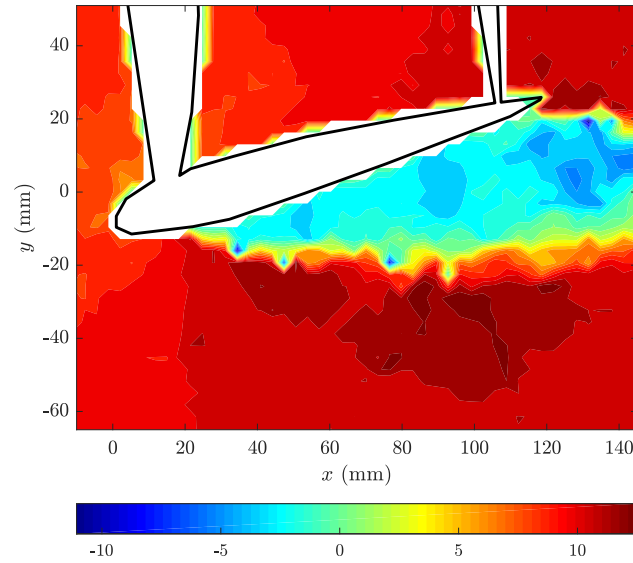
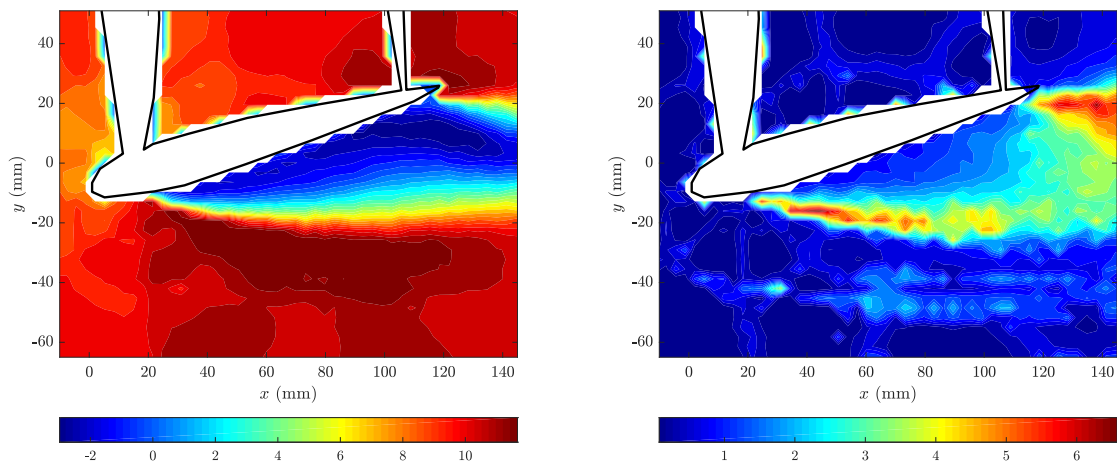


Figure 5.13: Instantaneous x -velocity contour computed at $\alpha = 15^\circ$, using a self-made PIV code.

The mean and RMS velocity contours are shown in figure 5.14. The general trend of these contours are similar to the contours obtained using the instructor code. In addition to the lower resolution of the images, the RMS velocity contour also indicates a lot more velocity variations. There are additional high velocity spots predicted in both in the region of the wake and outside of it. This can be attributed to the fact that the self-made code does not follow an iterative procedure while calculating the cross-correlations, which leads to a less accurate computation of the velocity field.



(a) Mean x -Velocity.

(b) RMS x -Velocity Fluctuation.

Figure 5.14: Statistical velocity contours computed at $\alpha = 15^\circ$, using a self-made PIV code.

Velocity Profiles

In this section, we compare the velocity profiles obtained using the instructor code and the self-made code. The mean and RMS velocity profiles for the airfoil at an angle of attack of $\alpha = 15^\circ$, at a position $x/c = 1.2$ are shown in figure 5.15. We see that the mean velocity profiles obtained from the two different codes are closely matched, with the self-made code predicting marginally lower values of the mean velocity. The RMS velocity profiles on the other hand vary in magnitude with respect to each other. While the two profiles follow a similar trend, the self made code predicts higher values of velocity.

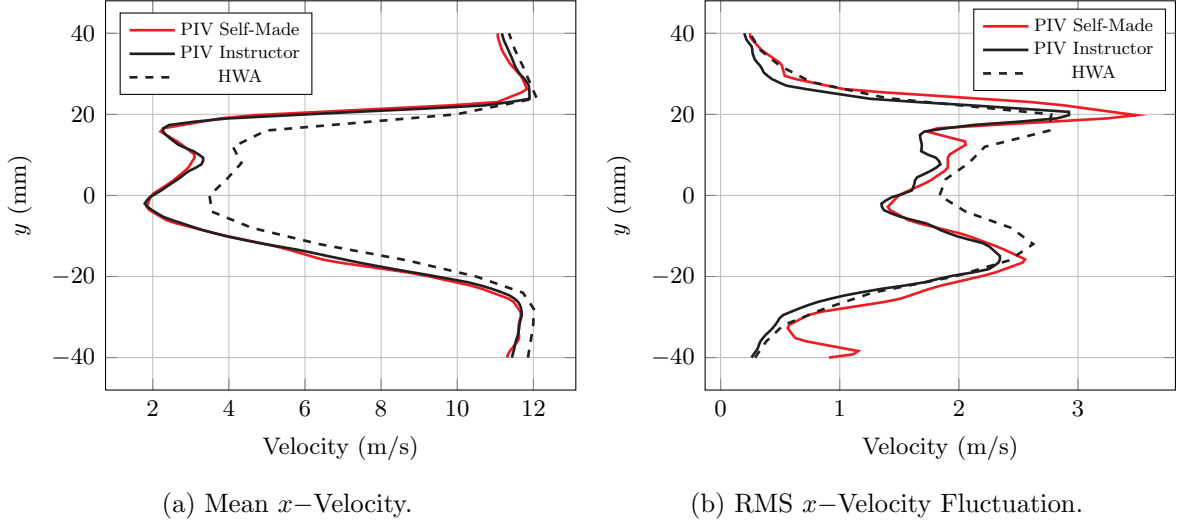


Figure 5.15: Velocity profiles at $x = 1.2c$, obtained using a self-made PIV code.

Advantages and Disadvantages of the self-made PIV code

The results obtained from the self-made code were analysed in the previous section. While the code captured the general trends of the velocity contours that are expected, it is limited in its accuracy due to the following reasons :

- The self-made code does not employ multiple iterations for the computations of the cross-correlations as opposed to the instructor code. The iterative procedure used in the instructor code increases the resolution which leads to a more accurate calculation of the velocity field.
- The instructor code employs window shifting and correlation window deformation, which when combined with the multiple iterations results in a better representation of the flow field as the local deformation of tracer particles are accounted for.
- The self-made code does not have a specific validation criterion to decrease the inaccurate velocity vectors.

Chapter 6

Conclusion

In this section, we look at the advantages and disadvantages of HWA and PIV with respect to each other. We also make some concluding remarks about the experiment and results obtained.

6.1 Advantages of HWA and PIV

HWA

- HWA is a relatively cheap and effective way to measure the speed of the wind tunnel. It does not require expensive material to set-up and can be easily operated by anyone.
- The analysis involves very little computational power. Once the calibration process is completed, the results can be obtained and process very quickly giving us close to real time data.
- The probe system can be easily modified or can be custom built for different experimental applications. This makes HWA a desirable choice for testing unique shapes and designs in a wind tunnel.

PIV

- PIV allows for the full flow field to be visualized. This is a huge advantage as it provides a more detailed look at the flow. It gives the chance to observe and analyze effects such as flow separation, flow reversal and vortex shedding by looking at the velocity contours.
- PIV is not intrusive, in that there are no instruments in the flow that might disturb it. With the only requirement being optical access, the PIV method relies on taking images of the flow and hence does not alter it.
- PIV also requires less time for calibration as compared to HWA since it does not depend on things such as curve fitting King's Law. PIV is also unaffected by external factors such as temperature and pressure changes.

6.2 Disadvantages of HWA and PIV

HWA

- HWA allows for flow measurement at fixed points depending on the measurement campaign. This also means that it may not be able to measure velocity gradients accurately in the domain of interest.
- HWA is an intrusive method as the probe is inserted into the flow to take measurements. Although the probes are designed to minimize their effect on the flow, this is still a factor of consideration while using HWA.
- In order to use HWA, the probe must be calibrated as per King's Law and this must be done before every measurement campaign as the probe is sensitive to the ambient pressure and temperature.
- The hot-wire is an extremely sensitive probe and must be carefully handled at all times in order to not break the wire. Additionally, the probe has limited spatial resolution which makes it harder to measure velocity distributions.

PIV

- Since it does not measure the flow directly, when it comes to supersonic and hypersonic flow, PIV might not be the best option for flow visualization and measurement.
- The need for perpendicular access is a limiting factor for PIV.
- PIV has a very complicated and expensive set up. It involves obtaining a computer system, laser system and an image processing software in order to collect and analyze the data. Additionally, the sheet position is of prime importance in order to get sharp images without shadows and reflections.
- PIV also involves a lot of data processing in that the two image frames must be cross-correlated in order to obtain the velocity. This can take up a lot of computational time.

6.3 Concluding Remarks on the Experiment

The aim of the lab exercise was to explore 2 techniques to measure the velocity of the flow around a NACA 0012 airfoil in a wind tunnel at various locations. The techniques investigated were Hot Wire Anemometry (HWA) and Particle Image Velocimetry (PIV). Post setup and calibration, the data for both techniques was processed using MATLAB.

For the HWA experiment, the data provided by the instructors was first calibrated as per King's Law. It was found that a 3^{rd} degree polynomial was the best fit. During the calibration process, the overheat ratio and optimal sampling frequencies were calculated. These were found to be 0.5 and 151.5152 Hz respectively. The experimental data was then processed for 3 different angles of attack, namely $\alpha = 0^\circ, 5^\circ$, and 10° . The data was then processed to find the velocity

(mean and RMS fluctuations) distributions at the respective angles of attack. The results obtained were in line with the flow physics of the NACA 0012 at the above mentioned angles of attack. It was found that at 15° , there was a significant amount of velocity reduction due to flow separation. Additionally, it also had the highest RMS velocity fluctuations. On the other hand, 0° and 5° showed lesser mean velocity reduction and RMS fluctuations, indicating a smoother wake.

In PIV, the experimental parameters like $f_{\#}$ and light pulse separation were determined based on the camera and then redefined using the magnification factor obtained through experimental calibration. The flow field was visualised for the 3 angles of attack using a code provided by the instructors and one that was self-made. While the professional code took longer computation time, it produced more accurate results. The effects of light pulse separation, interrogation window size and ensemble size were also looked into, the key takeaways being that a light pulse separation of $100\ \mu\text{s}$, interrogation windows that were 32×32 px and an ensemble size of 100 samples gave the best representation of the flow field..

It was observed that the results obtained through PIV were consistent with those obtained through HWA while providing more insight into the flow around the airfoil, particularly in the region of the turbulent wake at $\alpha = 15^\circ$. In general, PIV gave lower mean velocities than those measured through HWA. At low angles of attack, the root-mean-squared fluctuation obtained through PIV was higher than that obtained through HWA while this was reversed at the higher angle of attack of 15° . Comparing the two techniques, it is seen that HWA is a financially and computationally cost-effective way to measure the velocity of the flow at particular points of interest. For a better understanding of the development of the flow, especially when turbulence is involved, PIV is recommended.

References

- Kompenhans, J., Raffel, M., Dieterle, L., Dewhurst, T., Vollmers, H., Ehrenfried, K., ... others (2000). Particle image velocimetry in aerodynamics: Technology and applications in wind tunnels. *Journal of Visualization*, 2(3, 4), 229–244.
- Sciacchitano, A., & Scarano, F. (2021a). Flow measurement techniques: Course reader and slides.
- Sciacchitano, A., & Scarano, F. (2021b). Flow measurement techniques: Student manual for the laboratory exercise.
- Stornelli, V., Ferri, G., Leoni, A., & Pantoli, L. (2017). The assessment of wind conditions by means of hot wire sensors and a modified wheatstone bridge architecture. *Sensors and Actuators A: Physical*, 262, 130–139.